

A catalog of 1.5273 μm diffuse interstellar bands based on APOGEE *hot telluric* calibrators

M. Elyajouri,¹

meriem.el-yajouri@obspm.fr

A. Monreal-Ibero¹, Q. Remy² and R. Lallement¹

1 GEPI Observatoire de Paris, PSL Research University, CNRS, Université Paris-Diderot, Sorbonne Paris Cité

2 Laboratoire AIM, IRFU/Service d'Astrophysique CEA/DSM CNRS Université Paris Diderot

ABSTRACT

High resolution stellar spectroscopic surveys provide massive amounts of diffuse interstellar bands (DIBs) measurements. Data can be used to study the distribution of the DIB carriers and those environmental conditions that favor their formation. In parallel, recent studies have also proved that DIBs extracted from stellar spectra constitute new tools for building the 3D structure of the Galactic Interstellar Medium (ISM). The amount of details on the structure depends directly on the quantity of available lines of sight (LOS). Therefore there is a need to construct databases of high-quality DIB measurements as large as possible. We aim at providing the community with a catalog of high-quality measurements of the 1.5273 μm DIB towards a large fraction of the *Apache Point Observatory Galactic Evolution Experiment* (APOGEE) hot stars observed to correct for the telluric absorption and not used for ISM studies so far. This catalog would complement the extensive database recently extracted from the APOGEE observations and used for 3D ISM mapping. We devised a method to fit the stellar continuum of the hot calibration stars and extracted the DIB from the normalized spectrum. Severe selection criteria based on the absorption

¹5, Place Jules Janssen, 92195 Meudon, France

²Bat. 709, CEA-Saclay, 91191 Gif-sur-Yvette Cedex, France

characteristics are applied to the results. In particular limiting constraints on the DIB widths and Doppler shifts are deduced from the HI 21 cm measurements, following a new technique of decomposition of the emission spectra. From $\sim 16\,000$ available *hot telluric* spectra we have extracted ~ 6700 DIB measurements and their associated uncertainties. The statistical properties of the extracted absorptions are examined and our selection criteria are shown to provide a robust dataset. The resulting catalog contains the DIB total equivalent widths, central wavelengths and widths. We briefly illustrate its potential use for the stellar and interstellar communities.

Subject headings: ISM: lines and bands – dust– extinction

1. Introduction

The spectra of stars viewed through one or several interstellar clouds display a plethora of relatively weak non-stellar absorption features of unknown origin, the so-called Diffuse Interstellar Bands (DIBs, see Herbig 1995; Sarre 2006, for a review). First DIBs were discovered around the early 20's by Heger (see McCall & Griffin 2013, for a review of the history of the DIBs discovery) and their interstellar origin was established in the 30's (Merrill 1934, 1936). Today, more than 400 optical DIBs (400-900 nm) are known (e.g. Jenniskens & Desert 1994; Hobbs et al. 2009). The first near-infrared (NIR) DIB was discovered by Joblin et al. (1990). Currently, ~ 25 NIR DIBs have been identified (Foing & Ehrenfreund 1994; Geballe et al. 2011; Cox et al. 2014; Hamano et al. 2015, 2016), including the strong band at $1.318\ \mu\text{m}$. NIR DIBs are particularly useful since they allow to make use of highly reddened target stars and explore the densest areas of the ISM. Most measured DIBs have a Galactic origin. Still, they have also been detected in the Magellanic clouds, M31 and M33 (Welty et al. 2006; Cordiner et al. 2008a,b; Ehrenfreund et al. 2002; Cordiner et al. 2011; van Loon et al. 2013) and in a few line-of-sights towards e.g. starburst galaxies or in Type Ia supernovae spectra (Sollerman et al. 2005; Cox & Patat 2008; Heckman & Lehnert 2000; Phillips et al. 2013). Recently a DIB gradient was established for the first time in a 160 Mpc-distant galaxy (Monreal-Ibero et al. 2015).

In spite of the number and ubiquity of DIBs, the carrier of most DIBs (i.e. the agents that originate these features) remains unidentified. Carbon is involved in most of the proposed candidates and among them we can find hydrocarbon chains (e.g. Maier et al. 2004), polycyclic aromatic hydrocarbons (PAHs, e.g. van der Zwet & Allamandola 1985; Leger & D'Hendecourt 1985; Crawford et al. 1985; Salama et al. 1996; Kokkin et al. 2008), and/or fullerenes (Iglesias-Groth 2007; Sassara et al. 2001). See Cox (2011) for a recent review on

the DIB-PAH hypothesis. Today the situation is particularly promising in this regard, since the carrier for two DIBs at 9577 and 9632 Å was recently for the first time unequivocally identified with C_{60}^+ (Campbell et al. 2015), confirming earlier results of Foing & Ehrenfreund (1994). C_{60}^+ was also detected in emission towards NGC7023 by Berné et al. (2013), and C60 and C70 have also been identified in emission in young planetary nebulae (Cami et al. 2010). Besides, first insights on the physical properties of the environments that are favorable or not for DIB formation are being obtained from high-quality absorption data (Cox & Spaans 2006; Vos et al. 2011; Cordiner et al. 2013).

An interesting property of these features is that they are correlated with the amount of interstellar matter along the line of sight. Various correlations with neutral hydrogen, extinction and interstellar Na I D and Ca H&K lines have been established (e.g. Herbig 1993; Friedman et al. 2011). As a result, DIBs can be used to trace the structure of the ISM in the same way than others species, and they even offer certain advantages when used instead of (or in addition to) other tracers. For example, given their intrinsic weakness, they are ideal tracers in conditions where other features (e.g. Na I D) saturate, like very dense molecular clouds or regions seen through a large amount of extinction. Encouraged by this correlation between DIBs and IS matter, several teams have recently presented works that made use of the information provided by the different spectroscopic surveys to study the Galactic ISM structure and extinction in 2D or 3D by using the strength of different DIBs as a proxy (e.g. Yuan et al. 2014; Kos et al. 2014; Puspitarini et al. 2015; Lan et al. 2015; Baron et al. 2015).

In the near-IR, the 1.5273 μm band (hereafter, we will also use 15273 Å and refer to vacuum wavelengths) falls in the spectral range observed by the *Apache Point Observatory Galactic Evolution Experiment* (APOGEE, Wilson et al. 2010; Majewski 2012), and this high resolution, high signal, massive survey was used by Zasowski et al. (2015) to trace the 3D structure of the ISM at the large scale based on an unprecedented number of extracted NIR DIBs. Such pioneering work has demonstrated the potential of these methods and consequently that increasing the number of measurements will result in more accurate mapping.

In this article we present a work based on a fraction of the spectra of the most recent APOGEE’s target sample made publicly available. The entire dataset comprises $\sim 160\,000$ stars, most of them cool K and M giants ($T_{eff} \sim 3500 - 5000$ K). As part of the observing strategy and calibration plan of the survey, $\sim 17\,000$ *hot telluric* stars were also observed (see details in Sec. 2). By definition these are the bluest stars on a given pointing, and thus, most of the times early (i.e. O- to F-type) stars. As such, their almost featureless continua make them ideal targets to extract the information associated to the 1.5273 μm DIB. Our work has been focused on these calibration stars. We have devised a method to fit their

stellar continua and we present the resulting catalog of DIB measurements extracted from their spectra. This catalog complements the existing extensive catalog of Zasowski et al. (2015) based on the APOGEE main, cool targets.

The paper is structured as follows: Sect. 2 contains the technical aspects regarding the data used in this work. Sect. 3 describes the methods used for continuum fitting and DIB parameter extraction, whereas a detailed description of our criteria to validate a DIB detection and estimate uncertainties is included in Sect 4. Sect. 5 describes the resulting catalog and its validation. Sect. 6 illustrates some potential applications. Conclusions are summarized in Sect. 7.

2. The data

2.1. APOGEE overview

The SDSS-III *Apache Point Observatory Galactic Evolution Experiment* (APOGEE) is one of the four Sloan Digital Sky Survey III (SDSS-III, Eisenstein et al. 2011; Aihara et al. 2011) experiments operated from 2011 to 2014. APOGEE uses a 300-fiber multi-object spectrograph working in the near infrared (H -band, 1.51- 1.70 μm) at high spectral resolution ($R \sim 22\,500$, Wilson et al. 2010). The spectrograph is attached via a fiber optic train to the SDSS 2.5-meter telescope at Apache Point Observatory (Gunn et al. 2006). Since the effects of extinction at near-IR wavelengths are reduced, APOGEE has a strong potential to explore dust obscured regions of the Galaxy that are beyond the reach of optical surveys, in particular the inner Galaxy and bulge.

In a given observation, about 230 (out of 300) fibers are allocated for scientific targets selected from the source catalog the *Two Micron All Sky Survey* (2MASS, Skrutskie et al. 2006). The $\sim 160\,000$ selected scientific targets are distributed across all Galactic environments. Most of them are red giant stars but there are also special subsamples including stars with measured parameters and abundances from other spectroscopic studies, cluster members, etc. associated to several APOGEE ancillary science programs (see Zasowski et al. 2013, for a detailed description of the different target classes).

In addition to the science targets, a sample of hot stars, also called telluric standards stars (TSSs) or *hot telluric* calibrators are observed (35/300 fibers) to allow for the correction of the telluric absorption lines (see below). Finally, the remaining ~ 35 fibers are allocated for observing blank sky positions to enable sky emission subtraction.

2.2. The APOGEE telluric standard stars

The total number of TSSs in the APOGEE survey is nearly $\sim 17\,000$. Ideally, for a good telluric correction one would like to have bright O, B and A stars because of their featureless spectra. Therefore, to maximize the chances of observing stars of these types, the TSSs were selected as the bluest stars on a given plate having a magnitude in the range $5.5 \leq H \leq 11$ and ensuring a uniform distribution over the plate (see Zasowski et al. 2013, for details of TSS selection). Their spectra are used to adjust in an exquisite way the atmospheric transmission and its variability throughout the field, a transmission that is used to remove the telluric lines in all observed targets.

It is important to note that the TSSs are corrected for telluric absorption lines in the same way as the science targets. In other words, they benefit from the correction tool they have themselves produced. An interesting point about these stars is that, in addition to their use as tools to decontaminate the telluric absorption, they constitute a highly valuable dataset for ISM studies since their smooth continua are ideal to extract the information associated with DIBs. Here we focus on the strongest $1.5273\ \mu\text{m}$ DIB. Work is in progress on the weaker absorption bands.

The TSS can easily be identified in the APOGEE data products by means of the APOGEE_TARGET2 bitmask since all these stars are flagged as APOGEE_TELLURIC (bit 9).

2.3. Used information extracted from the APOGEE Archive

This work is based on the products from the SDSS data release 12 (DR12, Alam et al. 2015). This release includes all the data taken between April 2011 and July 2014. The spectra can be downloaded from the Science Archive Server (SAS) as described on the data access page ¹. There are three different types of reduced spectra available (see Nidever et al. 2015; Holtzman et al. 2015). Here, we use the calibrated, well-sampled, and pseudo continuum-normalized combined 1D spectra. These are available as fits files with four separate extensions: the first one carries the information about the star and the derived stellar parameters, the second one contains the observed spectra, the third one saves the error pixels and the fourth one has a state-of-the-art modeled spectrum S_λ adjusted to the observed one (García Pérez et al. 2015). The modeled spectra are interpolated from a grid of spectra, itself based on a large sample of model atmospheres (Mészáros et al. 2012). These modeled

¹http://data.sdss3.org/sas/dr12/apogee/spectro/redux/r5/stars/125_6d/v603/

spectra are optimized for stars at temperature $3\,800\text{ K} < T < 5\,250\text{ K}$ (Ahn et al. 2014). The TSSs are *a priori* hotter, and therefore as shown below, small adjustments to the provided modeled spectra were needed.

All the spectra are sampled at same rest wavelength pixel scale, with a constant dispersion in $\log \lambda$, as

$$\log \lambda_i = 4.179 + 6 \times 10^{-6} i \quad (1)$$

with 8575 total pixels ($i = 0$ to 8574), giving a rest wavelength range of 15 100.8 to 16 999.8 Å (Nidever et al. 2015).

We also use the table that summarizes all the parameters derived from the APOGEE spectra (for DR12, allStar-v603.fits), including for each observed individual star its mean barycentric radial velocity, the standard deviation of the mean velocity, the mean ASPCAP parameters and abundances as derived from the combined spectra, and a compilation of ancillary targeting data (see Nidever et al. 2015; Holtzman et al. 2015, for a full description of the data in these files).

3. Data analysis

The aim of this work is analyzing the series of $\sim 16\,000$ DR12 TSS spectra that can be downloaded from the APOGEE site to determine the presence (or absence) of the DIB at 15273 Å and measuring its equivalent width in case of positive detection. Given the volume of data, this needs to be done with as less as possible human intervention. For that, we took as starting point the methodology presented by Puspitarini et al. (2013) for optical spectra, and adapted it to the peculiarities of APOGEE spectra. At the end, we had a fully automated DIB extraction method able to measure DIB equivalent widths (EWs) without any user interaction during the fit. The code was developed using the IGOR PRO environment². Note that the reduced pseudo-normalized spectra of DR12 are corrected from telluric lines contamination. Thus, no telluric correction is needed. In the following, we give the details of our fitting technique, we explain how we extracted the EW of the DIB and how we estimated their associated uncertainties.

²<http://www.wavemetrics.com>

3.1. Profile fitting

We fit each TSS spectrum to a model made out of the product of several components as follows:

$$M_\lambda = [S_\lambda]^\alpha \times DIB[\sigma, \lambda, D] \times (1 + [A] \times \lambda) \quad (2)$$

with:

- $[S_\lambda]^\alpha$, *an adjusted stellar spectrum*: S_λ is the initial stellar model provided by the APOGEE project. As we mentioned above, this model is not optimized for the TSSs that are hotter than the main targets. Therefore, even if the velocity of each target star was accurately determined and the global shape of the spectrum was most of the times adequate, the depth of the stellar atmospheric lines was not properly estimated (see Figure 1). We included a scaling factor (α) in order to take this into account and to adjust the model depth to the data.

- $DIB[\sigma, \lambda_c, D]$, *the DIB profile*: It was modeled as a Gaussian function with three free parameters associated to its width (σ), central wavelength (λ_c) and depth (D).

- $(1 + [A] \times \lambda)$, *a local continuum*: this was a simple 1-degree polynomial introduced to model as closely as possible the continuum around the DIB.

We selected a pre-defined spectral range for the fit restricted to the vicinity of the DIB $[15\,260 - 15\,290]\text{\AA}$ to determine the above coefficients α , σ , λ_c , D and A . Note that this range was large enough to ensure an adequate sampling of the neighboring Brackett 19-4 stellar line at $1.52647\ \mu\text{m}$. Errors provided by APOGEE were used to mask those spectral ranges affected by artifacts due to imperfect sky emission correction or other sources of uncertainty. We use the Levenberg-Marquardt algorithm implemented in IGOR PRO to compute the coefficients that minimize the chi-square χ^2 . An example illustrating our fitting procedure is shown in Figure 1.

3.2. DIB equivalent width and error estimates

In the following, we explain how we extracted the DIB equivalent width from our fits and how we estimated the uncertainties associated to each of the parameters presented in the catalog.

- *Computation of the DIB equivalent width:* Since none of the previous or present observations reveals any asymmetry of the 15273 Å DIB, and for our sightlines the linear regime prevails, we assume that the actual DIB absorption has a shape that is similar to the mono-gaussian model. We also neglect the small departures from a Gaussian that result from multiple cloud superimposition that is small compared to other sources of uncertainties. Subsequently, assuming that the continuum $I_0(\lambda)$ is reasonably fitted, the DIB equivalent width (EW) is the area of the fitted Gaussian and can be simply analytically derived from its parameters as the product of the model DIB’s depth D by the coefficient σ :

$$EW = \int_{DIB} \frac{I_0 - I_\lambda}{I_0} d\lambda = \sqrt{2\pi} D \sigma \quad (3)$$

where $I(\lambda)$ is the observed spectrum.

- *Computation of standard deviations in residuals:* We calculated the standard deviation of the fit residuals, *data - model*, in a region close to the DIB (region A= $[\lambda_c - 10, \lambda_c + 10]$ Å). In addition to this, we performed a second fit using the same function as the one presented in equation 2 but over the whole spectral range covered by APOGEE. As a matter of fact, we found that the first and third terms of Equation 2 are good enough to represent continuum and Bracket lines in the entire APOGEE spectral region. For this fit the DIB term in the equation has the same restrictions as in the local fit. The DIB is fitted to ensure an optimum placement of the continuum in the DIB region and subsequently everywhere. As a matter of fact, omitting the DIB could bias the continuum in its spectral region and react on the whole fit. The residuals from this additional fit were used to obtain two additional measurements of the standard deviation. The first one was calculated over a *clean* (i.e. free from DIB absorption, strong stellar lines and telluric residuals) spectral range (region B= $[15\,892-15\,959]$ Å). The second one (region C= $[15\,200-15\,250]$ Å) corresponds to a region relatively close to the DIB (and also free of DIB) and potentially contaminated by stellar residuals.

Hereafter, we will call the standard deviation R for all the three regions, R_A , R_B and R_C . These were used for the selection criteria discussed in Section 4. Also, the standard deviation R_A in the narrow spectral range around the DIB is used below to estimate the uncertainty on the DIB equivalent width.

- *Uncertainties on the DIB central wavelength and width:* The IGOR algorithm uses data and fitted model to evaluate the *data–model* standard deviation in the spectral range used for the fit, within the implicit assumption that the fitting function is ideally adapted to the data and the data are characterized by random Gaussian noise. If there are telluric line residuals or any other artefacts that amplify the signal fluctuations, the estimated standard deviation is correspondingly increased and treated as random noise. Based on the standard deviation and the mutual influence of the parameters the algorithm estimates one sigma errors on each parameter. We use these error estimates on both the central wavelength and the width.

- *Uncertainty on the DIB equivalent width:* For this quantity we estimated the error in a very conservative way in order to take into account the departures from Gaussian noise and the ideal fitting function, as well as potential subsequent misplacements of the continuum level. As a matter of fact in a number of cases telluric absorption or sky emission correction residuals are present and for a number of targets the stellar line shapes are not perfectly fitted. This may result in slight displacements of the fitted continuum that do not impact the line center and impact the width in a negligible way but may impact the depth. For the most conservative estimate of the error we used the standard deviation of region A, coupled to the maximum DIB width deduced for each sightline from HI 21 cm data (see Sect. 4). The maximum error was estimated as the equivalent width of a Gaussian with the maximum width of the HI 21 cm line and a depth equal to R_A :

$$err(EW) = \sqrt{2\pi} R_A \sigma_{HI\,21cm} \quad (4)$$

We checked that this conservative error is appropriate to all types of spectra and data quality, including those cases where there are clear residuals linked to stellar or telluric lines. Figure shows the estimated error as a function of the equivalent width for all targets of the catalog. It can be seen from the figure that due to our method based on HI, for the same EW the error is significantly larger in directions where the ISM radial velocity range is very large, mainly here at Galactic longitudes smaller than 70 deg. This confirms that our quoted values are very conservative.

4. Validation criteria

4.1. Selection of fitted absorptions

We applied a series of tests to the fitted Gaussian absorptions based on the fitted parameters, the signal quality in the DIB region and elsewhere, and finally the LOS direction

and the corresponding Galactic gas. The series of tests is schematically represented in Figure 2.

- *First global test*: the first selective test eliminates those absorptions that are deeper than 10% of the continuum (arrow (a) in Figure 2). Those depths are extremely unlikely for Galactic DIBs and especially for the TSSs that are nearby. Indeed, we checked a posteriori that all those cases correspond to spurious detections (stellar lines for the coolest or most metallic objects, unusually strong telluric residuals, etc). We also eliminated simultaneously absorptions centered outside the spectral range [15268-15280] Å. In the red, the corresponding large Doppler shifts of $\geq +137\text{km s}^{-1}$ are unrealistic for the nearby ISM. In the blue, the test excludes a tiny fraction of fits with unrealistically high negative Doppler shifts caused by a stellar line (see the histogram in Figure 5).

- *Test on the absorption depth*: as a second test for the selected targets (the arrow (b)), we compared the depth of the fitted absorption line with the standard deviation on the residuals. This comparison was done in a one- or two-step process. We first compare the absorption depth with the maximum of the three standard deviations R_A , R_B and R_C described in section 3.2. If it is larger (arrow (d)), then start directly the tests on the width. If the depth is smaller than this maximum, i.e if the spectrum is globally too noisy to detect the DIB (the arrow (c)) or the DIB is very shallow, we also compared the absorption depth with the local standard deviation R_A only. This second step allows to detect those spectra that are noisy in those spectral ranges far from the DIB but that have a good enough signal to noise in the DIB neighborhood to ensure a detection, i.e. the use of the maximum of the three R_A , R_B and R_C deviations is too restrictive. Absorptions that pass successfully the test (arrow (e)) are then examined for their widths in the same way than the previous ones (arrow(d)) but are flagged differently. The difference in the flags serves to evaluate the quality of the spectrum and identify those targets for which models have a shape incompatible with the measurements outside the DIB region. They will be visually inspected one by one. Absorptions who still appear too shallow (arrow (g)) are examined in a different way.

- *Criterion on the width in case of shallow absorptions*: as a third test for those absorptions that appear small with respect to the noise, both locally and in the three spectral regions (i.e. from arrow (g)), we selected the DIBs with a width, σ , within predefined limits. The lower limit of 0.7 Å is deduced from the results of Zasowski et al. (2015) and in particular from the σ histogram of the whole APOGEE dataset shown in their Figure 6. This histogram shows that a very abrupt decrease occurs at $\simeq 1$ Å implying that the intrinsic DIB width maybe as small as this value. Taking into account our typical uncertainties on

the DIB width, $\text{err}(\sigma) \simeq 0.35$, we finally imposed a lower limit on the width of 0.7 \AA . This criterion has been checked a posteriori to eliminate spurious detections associated to bad pixels or telluric residuals, and simultaneously to keep actual detections of narrow DIBs. A typical example of such narrow absorptions that pass successfully the test is shown in Figure 3. It can be seen from the figure that it looks convincingly like an actual DIB. The upper limit of 1.0 \AA is chosen for the following reasons: for those absorptions that are very shallow (arrow (g)), this maximum value eliminates flat and elongated features of uncertain origin. Conversely, those very shallow absorptions that are reasonably wide pass the test and are falling in the *upper limit* category (yellow box in Figure 2). For those absorptions that are deeper and correspond to arrow (f), this maximum value will result in definitely rejecting those features that are broader than $1.5\sigma_{HI21cm}$ (see below).

- *Limits on the width σ based on HI 21cm emission spectra:* For all absorptions that exceed the noise level, either globally or locally (arrows (d) and (e)), a subsequent test on the DIB width is performed based on radio 21cm HI spectra. As a matter of fact the velocity range for some fitted absorptions is clearly not compatible with the velocity distribution in the Galaxy. Such unrealistic absorption widths are caused by an improper modeling of the stellar lines, residuals of telluric lines, or a locally increased level of noise. In order to eliminate these spurious or biased detections from the catalog we added the following constraint on the DIB width based on the radial velocities of the atomic hydrogen gas. Indeed as the HI is the most common and widespread form of gas in the galaxy, its extent in velocity should encompass the velocity extent of the DIB, as verified in previous DIB measurements (see e.g. Puspitarini et al. 2015; Zasowski et al. 2015).

We estimated the maximal radial velocity width of the DIB by constructing a *virtual*, composite DIB based on the HI spectra. To do so we used the results of the HI line decomposition method presented in Planck et al. (2015). We briefly recall the principle of this decomposition. The first step is to detect the significant lines in the brightness temperature $T_B(v)$ spectra of the LAB Survey (Kalberla et al. 2005). We measured the dispersion in temperature, T_{rms} , outside the bands with significant emission. In order to limit the number of false detections caused by strong noise fluctuation we clipped the data to zeros except if $T_B(v) > T_{rms}$ in 3 channels (3 km s^{-1}). Then, using the 5-point-Lagrangian differentiation twice, we computed the curvature d^2T_B/dv^2 in each channel. Lines are detected as negative minima in d^2T_B/dv^2 . False detections triggered by the edges of the clipped regions were eliminated. Then each spectrum is fitted by a sum of pseudo-Voigt functions, one for each detected line. The pseudo-Voigt function is defined as

$$\text{PV} = \eta\text{L} + (1 - \eta)\text{G} \tag{5}$$

with $0 < \eta < 1$ the shape factor, L a Lorentzian, and G a Gaussian respectively defined as :

$$L = \frac{h}{1 + \left(\frac{v-v_0}{\sigma}\right)^2} \quad (6)$$

and,

$$G = h \exp\left(-\frac{(v-v_0)^2}{\sigma}\right) \quad (7)$$

where v_0 is the position of the line, σ the width and h the height parameter.

In order to take into account the detection uncertainties, the position of the line v_0 is allowed to vary in a $\pm 4 \text{ km s}^{-1}$ range around the initial position. For each detected line the free parameters η , h , σ , and v_0 are fitted by means of a χ^2 minimization.

For each LOS the computed HI decomposition is used to construct a *virtual* DIB, the one that would be measured in the spectrum of a star located beyond all the HI clouds, i.e. at the periphery of the Galactic HI disk. To do so, each HI component is associated to a DIB that has a width $\sigma_0 = 1.4 \text{ \AA}$ and a radial velocity equal to the one of the HI line. The chosen width σ_0 corresponds to an upper limit on the intrinsic DIB width that can be derived from the Figure 6 of Zasowski et al. (2015). To convert the HI line into a DIB equivalent width we use the following relationships:

- i) The HI column density is calculated in the optically thin limit:

$$N_{HI} = 1.823 \times 10^{18} \int T_b(v) dv \quad (8)$$

where $T_b(v)$ is the 21 cm line brightness temperature at radial velocity v .

- ii) The HI column density is transformed into reddening using the $N_{HI} - E(B - V)$ empirical relation from Gudennavar et al. (2012) and the average $R_v = A_v/E(B - V)$ value of =3.1:

$$A_v = 3.1 \times 1.6 \times 10^{-22} \times N_{HI} \quad (9)$$

and finally

- iii) The extinction is converted into a DIB equivalent width using the relation derived by Zasowski et al. (2015):

$$EW_{DIB} = 0.102 \times A_v^{1.01} (\text{\AA}) \quad (10)$$

The depth of each individual DIB is computed from the EW and the width. The final *virtual* DIB is the product of those individual DIBs and as such it is broadened to match

the velocity distribution of the HI spectrum for the entire path through the Galaxy. Figure 4 illustrates the construction of the *virtual* DIB for a typical LOS with 6 HI clouds. This *virtual* DIB is fitted to a Gaussian and the resulting width σ_{HI21cm} is used to impose a limit on the APOGEE absorption width. Such a limit is ensuring the compatibility between the measured DIB width and the velocity spread seen in HI. Absorptions that do not pass the test (i) as shown in Figure 2 enter test (f). The broad absorptions will be discarded as discussed above and the narrow lines are reconsidered and classified as shown in Figure 2.

4.2. Special cases

We applied target selection criteria and considered separately Be Stars and stars from the field 4529 because they can yield difficulties in fitting. To do so we used the Chojnowski et al. (2015) catalog of Be stars and the information contained in the APOGEE tables. All these spectra have been the subject of one by one visual inspection and only those where the DIB was clearly unambiguously and accurately detected were kept. Figure 14 contains an example of a Be star spectrum and a spectrum from a star in plate 4259.

The different possible outcomes after the selection criteria described in section 4.1 and 4.2 have been flagged from 1 to 7. Figure 14 presents one representative example for each category.

5. The catalog

A fraction of the catalog of all detected DIBs is presented in Tab. 2 while a summary of its statistical properties appears in Tab. 1. For the total of 6 716 detections or upper limits the catalog lists the 2MASS identification, then the equivalent width, central wavelength and DIB Gaussian width and associated errors. The flag allowing to identify the selection criteria for each target is also added. Finally, we included for completeness the estimated equivalent width for the *virtual DIB* as calculated from the emission in the HI 21 cm line. The various categories (1) Upper limit (2) Stars from plate 4529 (3) Be Stars (4) Narrow recovered DIBs (5) Narrow DIBs (6) Recovered (7) Detected comprise 362, 11, 52, 122, 473, 572 and 5124 TSS targets respectively. Figure 10 shows the location of all TSSs on a sky coordinates plot, distinguishing those that are included in the catalog. It can be seen that at Galactic latitudes smaller than $\simeq 15$ degrees all APOGEE fields contain TSSs with detected DIBs, while at higher latitude some fields have no targets included in this catalog, due to

the weakness of the IS column.

Table 1: Summary with statistics of the selected sample

	λ_c (Å)	σ (Å)	EW (mÅ)
Mean	15272.42	1.50	78
Std Dev	1.13	0.40	49
Median	15272.43	1.47	69

The comparison between the velocity distributions of the original sample and the one included in this catalog is presented in Figure 5. Both of them peak at ~ -20 km s $^{-1}$. However, while the final distribution resembles to a Gaussian distribution, the original one is quite irregular, with several secondary peaks. In particular those at ~ -260 and -130 km s $^{-1}$ correspond to very strong stellar absorption features that have been successfully eliminated. Note that the final sample presents a relatively small (i.e. $\lesssim 30$) number of detections with high velocities (i.e. ~ 100 km s $^{-1}$). After visual inspection of the corresponding spectra, we did not see any evidence for a spurious detection. Therefore we kept those detections in the catalog. They will be the subject of further work. We cannot exclude a similar high velocity tail in the blue due to the threshold imposed to remove spurious identifications due to stellar lines.

Figure 6 displays the distribution of the DIB widths. Only a very small fraction of selected DIBs have sigma above 3 Å. In the same way, Figure 7 shows that there are very few DIBs (~ 167) with equivalent width > 200 mÅ. This is not unexpected since TSS are relatively nearby stars, much closer than the APOGEE targets full sample. Finally, we show in Figure 8 a comparison between the APOGEE measured EWs and the EWs of the *virtual* DIBs described in section 4 that are proportional to the total hydrogen column from the LAB Survey (Kalberla et al. 2005), converted into an equivalent width according to equation 4. The figure shows that, within the error bars, there is an envelope to all the data points that corresponds roughly to a one-to-one relation. This supports the robustness of our method and the choice of the conversion factor. Data points close to the envelope very likely correspond to target stars located beyond all the HI clouds seen in emission, while points well below the envelope correspond to targets that are in front of at least one cloud.

Table 2. Sample stars with 15 273 Å DIB detection.

2MASS ID	GLON	GLAT	$\lambda_c \pm err(\lambda)$	$\sigma \pm err(\sigma)$	$EW \pm err(EW)$	Flag	$EW_{HI\ 21cm}$
00001687 + 5903034	116.390	-03.169	15274.0 ± 0.2	1.1 ± 0.2	041 ± 018	7	219
00001877 + 5938132	116.500	-02.595	15272.3 ± 0.1	1.4 ± 0.1	075 ± 019	7	231
00005414 + 5522241	115.740	-06.791	15271.1 ± 0.3	1.9 ± 0.3	058 ± 018	7	109
00010331 + 1549325	105.570	-45.340	15272.0 ± 0.4	0.8 ± 0.5	010 ± 021	1	017
00010512 + 5651581	116.060	-05.332	15271.9 ± 0.4	1.4 ± 0.4	027 ± 014	6	148
00011569 + 6314329	117.320	+00.919	15274.5 ± 0.1	1.5 ± 0.2	097 ± 020	7	313
00013391 + 5904490	116.550	-03.172	15272.2 ± 0.1	0.9 ± 0.1	042 ± 022	5	219
00013919 + 7005554	118.690	+07.639	15272.8 ± 0.2	1.6 ± 0.2	062 ± 011	7	187
00022269 + 6254032	117.380	+00.559	15273.5 ± 0.1	2.0 ± 0.2	128 ± 025	7	279
00023939 + 7109185	118.970	+08.659	15271.7 ± 0.3	1.7 ± 0.3	053 ± 010	7	138
00024298 + 5748303	116.460	-04.450	15272.4 ± 0.2	1.2 ± 0.2	033 ± 016	7	190
00024671 + 1605384	106.240	-45.194	15272.8 ± 0.2	0.7 ± 0.2	016 ± 012	5	017
00024931 + 5709106	116.350	-05.096	15272.7 ± 0.3	1.7 ± 0.3	049 ± 013	6	158
00024931 + 5709106	116.350	-05.096	15272.7 ± 0.2	1.3 ± 0.2	058 ± 017	7	158
00025231 + 5841372	116.650	-03.584	15272.9 ± 0.2	1.8 ± 0.2	069 ± 017	7	223
00025606 + 7014169	118.820	+07.754	15273.2 ± 0.3	1.2 ± 0.3	029 ± 013	7	164
00032397 + 7310282	119.420	+10.631	15268.4 ± 0.5	0.8 ± 0.6	008 ± 016	1	103
00042334 + 5626552	116.430	-05.828	15273.0 ± 0.2	0.8 ± 0.2	024 ± 022	4	141
00044189 + 6939114	118.860	+07.152	15274.4 ± 0.3	0.9 ± 0.3	021 ± 013	4	216
00044627 + 0132128	099.672	-59.211	15271.4 ± 0.6	0.9 ± 0.6	008 ± 009	1	013
00045177 + 5933503	117.060	-02.775	15272.5 ± 0.4	2.2 ± 0.4	066 ± 027	7	230
00045306 + 7048114	119.090	+08.280	15273.6 ± 0.8	1.4 ± 0.8	014 ± 007	6	138
00050083 + 6349330	117.840	+01.414	15271.9 ± 0.1	2.0 ± 0.1	175 ± 030	7	313
00051293 + 5811530	116.860	-04.127	15272.7 ± 0.1	1.2 ± 0.1	060 ± 013	7	223
00051873 + 5758464	116.830	-04.345	15274.0 ± 0.2	1.6 ± 0.2	070 ± 024	7	193
00052394 + 6347207	117.870	+01.370	15271.9 ± 0.1	1.7 ± 0.1	135 ± 019	7	313
00052888 + 5717190	116.730	-05.028	15272.0 ± 0.3	1.2 ± 0.3	026 ± 014	7	158
00052965 + 5722141	116.750	-04.948	15272.3 ± 0.3	1.4 ± 0.3	043 ± 024	7	158
00053673 + 7530446	120.010	+12.901	15272.2 ± 0.2	1.7 ± 0.2	082 ± 023	7	110
00054538 + 6234237	117.700	+00.167	15274.7 ± 0.1	1.4 ± 0.1	133 ± 029	7	293
00060064 + 7001540	119.040	+07.504	15271.3 ± 0.3	1.4 ± 0.3	036 ± 011	7	193
00060945 + 6412287	118.030	+01.768	15272.1 ± 0.1	1.7 ± 0.1	130 ± 023	7	335
00061415 + 0127198	100.290	-59.414	15271.8 ± 0.2	0.8 ± 0.2	023 ± 016	5	014
00063033 + 5719168	116.870	-05.021	15272.8 ± 0.2	0.8 ± 0.2	021 ± 015	5	172
00064418 + 7541165	120.110	+13.062	15271.0 ± 0.4	2.3 ± 0.4	071 ± 026	6	110
00064478 + 0025574	099.822	-60.418	15271.6 ± 0.2	0.7 ± 0.2	024 ± 017	4	019
00064971 + 5737102	116.970	-04.734	15272.7 ± 0.4	2.1 ± 0.5	048 ± 016	7	193
00065832 + 5726544	116.960	-04.906	15272.2 ± 0.4	1.8 ± 0.4	040 ± 017	7	172
00071354 + 5804306	117.100	-04.295	15272.8 ± 0.2	1.2 ± 0.2	041 ± 023	7	193
00072008 + 6241381	117.900	+00.254	15272.9 ± 0.1	1.4 ± 0.1	139 ± 033	7	296
00074256 + 6318026	118.040	+00.845	15271.3 ± 0.1	1.4 ± 0.1	120 ± 022	7	304
00074657 + 5722435	117.050	-04.993	15272.0 ± 0.2	1.4 ± 0.3	043 ± 014	7	172
00074863 + 7040220	119.310	+08.109	15271.7 ± 0.6	0.9 ± 0.6	009 ± 010	4	167
00080292 + 7332356	119.820	+10.934	15271.8 ± 0.2	0.9 ± 0.2	025 ± 022	3	099
00081304 + 6315383	118.090	+00.796	15273.9 ± 0.1	1.3 ± 0.1	085 ± 023	7	304

6. Potential applications

In the following, we illustrate the potential of this catalog by means of two examples: as a proxy for the extinction and as tool for ISM tomography.

The 15 273 Å DIB is correlated with the extinction over at least three orders of magnitudes (Zasowski et al. 2015). Thus, it can be used as an independent approach to estimate it or as an initial guess in absence of better information. We crossmatched the present TSS catalog with the compilation of reddening measurements provided by Lallement et al. (2014) used to build local 3D maps of the ISM. Figure 11 shows the comparison between the APOGEE 1.5273 μm DIB equivalent width and the reddening for the 221 stars in common. There is a clear positive correlation showing that the fitted absorptions contain valuable information on the intervening ISM. The figure also presents the linear fit derived by Zasowski et al. (2015) for the APOGEE cool stars. Our data points cluster around this relationship in solid agreement with the results obtained for the late-type stars. We note however that the number of *outliers* with very weak DIBs is significantly higher than the number of *outliers* with strong DIBs. A possible explanation to this trend could be that UV radiation field of the early-type stars acts on the intervening matter. This influence of the star temperature has already been noticed in the past (Raimond et al. 2012; Vos et al. 2011).

Likewise, the catalog can be crossmatched with spectra available for the targets. Being relatively bright many of them have been the subject of specific investigations, allowing comparisons with other DIBs and atomic or molecular lines. We have found at least 100 targets that have been observed at very high resolution and are available from public archives.

Finally, as mentioned in the introduction, our main interest in this (or similar) catalogs is the potential for use in ISM tomography. Compared with the extended catalog of Zasowski et al. (2015) that allows mapping the Galactic scales, the TSSs are more appropriate for the

Table 2—Continued

2MASS ID	GLON	GLAT	$\lambda_c \pm err(\lambda)$	$\sigma \pm err(\sigma)$	$EW \pm err(EW)$	Flag	$EW_{HI\ 21cm}$
00085840 – 0015231	100.410	–61.257	15273.3 ± 2.5	0.9 ± 2.7	002 ± 014	1	016
00090905 + 5737124	117.270	–04.786	15271.8 ± 0.2	0.9 ± 0.2	036 ± 015	5	177
00091817 + 7022314	119.380	+07.795	15272.6 ± 0.2	1.2 ± 0.2	038 ± 011	7	167
00092728 + 7447408	120.130	+12.152	15271.4 ± 0.2	0.9 ± 0.2	038 ± 012	5	108
00094423 + 0117063	101.810	–59.865	15272.6 ± 0.4	1.7 ± 0.5	033 ± 014	7	013

Note. — Table 2 is published in its entirety in the electronic edition of the *Astrophysical Journal*. A portion is shown here for guidance regarding its form and content.

nearby ISM. As a proof-of-concept we explored this use in the Taurus-Perseus region. This is illustrated in Figure 12 that shows the dust optical thickness measured by Planck in this area (Planck Collaboration et al. 2014). Superimposed on the map are the TSS targets color-coded according to the detection (or non-detection) of a DIB with an equivalent width higher than 50 m\AA . The strength of the DIB is always small in regions with negligible or small dust emission while the contrary is seen towards opaque clouds. We selected two regions, marked as A and B in Figure 12, to explore the use of this catalog to locate the molecular clouds along the line of sight. For that, we used the subset of targets in these areas with Hipparcos parallax (Perryman et al. 1997; van Leeuwen 2007). Figure 13 shows a comparison between the detection (or absence) of a DIB towards a given target and the distance to it. For both cases there is a clear cut-off in distance between these two categories. This allows to bracket the distance to the main absorbing cloud: targets without detection are in front of the clouds while those with detection are well beyond. For our particular cases the main clouds are at about 150 pc, in agreement with the detailed tomography of Schlafly et al. (2014). This illustrates the potential of this catalog to build detailed 3D maps of the ISM once the more accurate and numerous parallaxes provided by Gaia will become available.

7. Summary and perspectives

We have analyzed the series of SDSS/APOGEE NIR spectra of the calibration stars used to decontaminate data from telluric absorption lines. Those targets are generally blue stars and the APOGEE *Stellar Parameters and Chemical Abundances Pipeline* (ASPCAP, García Pérez et al. (2015)) stellar models cannot be used straight away. We have used them as a starting point and allowed the model broad stellar features to vary in depth to reproduce the observed continuum. In the region of the $1.5273 \mu\text{m}$ DIB this adjustment has proven to be good enough to allow the extraction of the DIB equivalent width and central radial velocity through Gaussian fitting of the DIB absorption. Careful and severe examinations of the DIB parameters, the continuum shape and the quality of the adjustment were done. This results in a conservative selection of reliable DIB parameters. In particular all DIB candidates that contradict radial velocity limiting values based on the HI 21 cm spectra have been excluded. A total of 6 716 lines of sight are selected and the results are presented in a catalog that will be available from CDS, Strasbourg. The statistical properties of the resulting DIB database show that our selection criteria are fully appropriate.

Since most of the calibration stars are nearby objects (say, within the first kpc), such a DIB catalog can be used to improve 3D maps of the nearby ISM and to complement maps at larger scale. We have compared our DIB detections in the Taurus-Perseus region

with the distribution of dust as traced by Planck, finding a good agreement between the strength/existence of the DIBs and the location of the clouds in the plane of the sky. Likewise, we showed how used jointly with existing parallax (i.e. distances) of the stars they can be used to assign a distance to the clouds. A step forward would be the application to the DIBs of inversion methods to recover the 3D structure, as already attempted based on optical absorption lines and extinction (e.g. Vergely et al. 2010; Lallement et al. 2014; Sale & Magorrian 2014). A strong advantage of NIR DIBs is the potential use of highly reddened target stars and the exploration of dense IS clouds. Moreover, nowadays instrumentation is becoming more and more NIR-IR oriented and large datasets in this spectral range are foreseen. 3D maps of the Galactic ISM are tools of wide use and their quality is expected to increase considerably in future once the Gaia distances will be available. Independently, DIB-based maps can be compared with dust and gas 3D distributions, providing new diagnostics of the conditions of their formation, ionization and destruction. They can also help interpreting small-structure of ISM clouds and of UV radiation impact on DIBs revealed by high spatial or temporal resolution spectroscopic data (Cordiner et al. 2013; Smith et al. 2013).

R.L., A.M.-I. and Q.R. acknowledge support from Agence Nationale de la Recherche through the STILISM project (ANR-12-BS05-0016-02). M.ElJ. acknowledges funding from the Region Ile-de-France through the DIM-ACAV project.

Funding for the Sloan Digital Sky Survey IV has been provided by the Alfred P. Sloan Foundation, the U.S. Department of Energy Office of Science, and the Participating Institutions. SDSS-IV acknowledges support and resources from the Center for High-Performance Computing at the University of Utah. The SDSS web site is www.sdss.org.

SDSS-IV is managed by the Astrophysical Research Consortium for the Participating Institutions of the SDSS Collaboration including the Brazilian Participation Group, the Carnegie Institution for Science, Carnegie Mellon University, the Chilean Participation Group, the French Participation Group, Harvard-Smithsonian Center for Astrophysics, Instituto de Astrofísica de Canarias, The Johns Hopkins University, Kavli Institute for the Physics and Mathematics of the Universe (IPMU) / University of Tokyo, Lawrence Berkeley National Laboratory, Leibniz Institut für Astrophysik Potsdam (AIP), Max-Planck-Institut für Astronomie (MPIA Heidelberg), Max-Planck-Institut für Astrophysik (MPA Garching), Max-Planck-Institut für Extraterrestrische Physik (MPE), National Astronomical Observatory of China, New Mexico State University, New York University, University of Notre Dame, Observatório Nacional / MCTI, The Ohio State University, Pennsylvania State University, Shanghai Astronomical Observatory, United Kingdom Participation Group, Universidad Nacional Autónoma de México, University of Arizona, University of Colorado Boulder, University of Oxford, University of Portsmouth, University of Utah, University of Virginia,

University of Washington, University of Wisconsin, Vanderbilt University, and Yale University.

REFERENCES

- Ahn, C. P., Alexandroff, R., Allende Prieto, C., et al. 2014, *ApJS*, 211, 17
- Aihara, H., Allende Prieto, C., An, D., et al. 2011, *ApJS*, 193, 29
- Alam, S., Albareti, F. D., Allende Prieto, C., et al. 2015, *ApJS*, 219, 12
- Baron, D., Poznanski, D., Watson, D., Yao, Y., & Prochaska, J. X. 2015, *MNRAS*, 447, 545
- Berné, O., Mulas, G., & Joblin, C. 2013, *A&A*, 550, L4
- Cami, J., Bernard-Salas, J., Peeters, E., & Malek, S. E. 2010, *Science*, 329, 1180
- Campbell, E. K., Holz, M., Gerlich, D., & Maier, J. P. 2015, *Nature*, 523, 322
- Chojnowski, S. D., Whelan, D. G., Wisniewski, J. P., et al. 2015, *AJ*, 149, 7
- Cordiner, M. A., Cox, N. L. J., Evans, C. J., et al. 2011, *ApJ*, 726, 39
- Cordiner, M. A., Cox, N. L. J., Trundle, C., et al. 2008a, *A&A*, 480, L13
- Cordiner, M. A., Fossey, S. J., Smith, A. M., & Sarre, P. J. 2013, *ApJ*, 764, L10
- Cordiner, M. A., Smith, K. T., Cox, N. L. J., et al. 2008b, *A&A*, 492, L5
- Cox, N. L. J. 2011, in *EAS Publications Series*, Vol. 46, *EAS Publications Series*, ed. C. Joblin & A. G. G. M. Tielens, 349–354
- Cox, N. L. J., Cami, J., Kaper, L., et al. 2014, *A&A*, 569, A117
- Cox, N. L. J., & Patat, F. 2008, *A&A*, 485, L9
- Cox, N. L. J., & Spaans, M. 2006, *A&A*, 451, 973
- Crawford, M. K., Tielens, A. G. G. M., & Allamandola, L. J. 1985, *ApJ*, 293, L45
- Ehrenfreund, P., Cami, J., Jiménez-Vicente, J., et al. 2002, *ApJl*, 576, L117
- Eisenstein, D. J., Weinberg, D. H., Agol, E., et al. 2011, *AJ*, 142, 72
- Foing, B. H., & Ehrenfreund, P. 1994, *Nature*, 369, 296

- Friedman, S. D., York, D. G., McCall, B. J., et al. 2011, *ApJ*, 727, 33
- García Pérez, A. E., Allende Prieto, C., Holtzman, J. A., et al. 2015, ArXiv e-prints, arXiv:1510.07635
- Geballe, T. R., Najarro, F., Figer, D. F., Schlegelmilch, B. W., & de La Fuente, D. 2011, *Nature*, 479, 200
- Gudennavar, S. B., Bubbly, S. G., Preethi, K., & Murthy, J. 2012, *ApJS*, 199, 8
- Gunn, J. E., Siegmund, W. A., Mannery, E. J., et al. 2006, *AJ*, 131, 2332
- Hamano, S., Kobayashi, N., Kondo, S., et al. 2015, *ApJ*, 800, 137
- . 2016, *ApJ*, 821, 42
- Heckman, T. M., & Lehnert, M. D. 2000, *ApJ*, 537, 690
- Heger, M. L. 1922, *Lick Observatory Bulletin*, 10, 141
- Herbig, G. H. 1993, *ApJ*, 407, 142
- . 1995, *ARA&A*, 33, 19
- Hobbs, L. M., York, D. G., Thorburn, J. A., et al. 2009, *ApJ*, 705, 32
- Holtzman, J. A., Shetrone, M., Johnson, J. A., et al. 2015, *AJ*, 150, 148
- Iglesias-Groth, S. 2007, *ApJl*, 661, L167
- Jenniskens, P., & Desert, F.-X. 1994, *A&As*, 106
- Joblin, C., D’Hendecourt, L., Leger, A., & Maillard, J. P. 1990, *Nature*, 346, 729
- Kalberla, P. M. W., Burton, W. B., Hartmann, D., et al. 2005, *A&A*, 440, 775
- Kokkin, D. L., Troy, T. P., Nakajima, M., et al. 2008, *ApJl*, 681, L49
- Kos, J., Zwitter, T., Wyse, R., et al. 2014, *Science*, 345, 791
- Lallement, R., Vergely, J.-L., Valette, B., et al. 2014, *A&A*, 561, A91
- Lan, T.-W., Ménard, B., & Zhu, G. 2015, *MNRAS*, 452, 3629
- Leger, A., & D’Hendecourt, L. 1985, *A&A*, 146, 81
- Maier, J. P., Walker, G. A. H., & Bohlender, D. A. 2004, *ApJ*, 602, 286

- Majewski, S. R. 2012, in American Astronomical Society Meeting Abstracts, Vol. 219, American Astronomical Society Meeting Abstracts #219, 205.06
- McCall, B. J., & Griffin, R. E. 2013, in Proceedings of the royal society A, Vol. 469, Proceedings of the royal society A, ed. M. Berry, 20120604
- Merrill, P. W. 1934, PASP, 46, 206
- . 1936, ApJ, 83, 126
- Mészáros, S., Allende Prieto, C., Edvardsson, B., et al. 2012, AJ, 144, 120
- Monreal-Ibero, A., Weilbacher, P. M., Wendt, M., et al. 2015, A&A, 576, L3
- Nidever, D. L., Holtzman, J. A., Allende Prieto, C., et al. 2015, AJ, 150, 173
- Perryman, M. A. C., Lindgren, L., Kovalevsky, J., et al. 1997, A&A, 323
- Phillips, M. M., Simon, J. D., Morrell, N., et al. 2013, ApJ, 779, 38
- Planck, Fermi Collaborations, Ade, P. A. R., et al. 2015, A&A, 582, A31
- Planck Collaboration, Abergel, A., Ade, P. A. R., et al. 2014, A&A, 571, A11
- Puspitarini, L., Lallement, R., & Chen, H.-C. 2013, A&A, 555, A25
- Puspitarini, L., Lallement, R., Babusiaux, C., et al. 2015, A&A, 573, A35
- Raimond, S., Lallement, R., Vergely, J. L., Babusiaux, C., & Eyer, L. 2012, A&A, 544, A136
- Salama, F., Bakes, E. L. O., Allamandola, L. J., & Tielens, A. G. G. M. 1996, ApJ, 458, 621
- Sale, S. E., & Magorrian, J. 2014, MNRAS, 445, 256
- Sarre, P. J. 2006, Journal of Molecular Spectroscopy, 238, 1
- Sassara, A., Zerza, G., Chergui, M., & Leach, S. 2001, ApJS, 135, 263
- Schlafly, E. F., Green, G., Finkbeiner, D. P., et al. 2014, ApJ, 786, 29
- Skrutskie, M. F., Cutri, R. M., Stiening, R., et al. 2006, AJ, 131, 1163
- Smith, K. T., Fossey, S. J., Cordiner, M. A., et al. 2013, MNRAS, 429, 939
- Sollerman, J., Cox, N., Mattila, S., et al. 2005, A&A, 429, 559
- van der Zwet, G. P., & Allamandola, L. J. 1985, A&A, 146, 76

- van Leeuwen, F. 2007, *A&A*, 474, 653
- van Loon, J. T., Bailey, M., Tatton, B. L., et al. 2013, *A&A*, 550, A108
- Vergely, J.-L., Valette, B., Lallement, R., & Raimond, S. 2010, *A&A*, 518, A31
- Vos, D. A. I., Cox, N. L. J., Kaper, L., Spaans, M., & Ehrenfreund, P. 2011, *A&A*, 533, A129
- Welty, D. E., Federman, S. R., Gredel, R., Thorburn, J. A., & Lambert, D. L. 2006, *ApJS*, 165, 138
- Wilson, J. C., Hearty, F., Skrutskie, M. F., et al. 2010, in *Society of Photo-Optical Instrumentation Engineers (SPIE) Conference Series*, Vol. 7735, *Society of Photo-Optical Instrumentation Engineers (SPIE) Conference Series*, 1
- Yuan, H.-B., Liu, X.-W., Xiang, M.-S., et al. 2014, in *IAU Symposium*, Vol. 298, *IAU Symposium*, ed. S. Feltzing, G. Zhao, N. A. Walton, & P. Whitelock, 240–245
- Zasowski, G., Johnson, J. A., Frinchaboy, P. M., et al. 2013, *AJ*, 146, 81
- Zasowski, G., Ménard, B., Bizyaev, D., et al. 2015, *ApJ*, 798, 35

A. Various categories of selected absorptions

The various types of detections or upper limits resulting from the criteria shown in Figure 2 are illustrated in Figure 14. We assigned a flag in the catalog to each of the different categories.

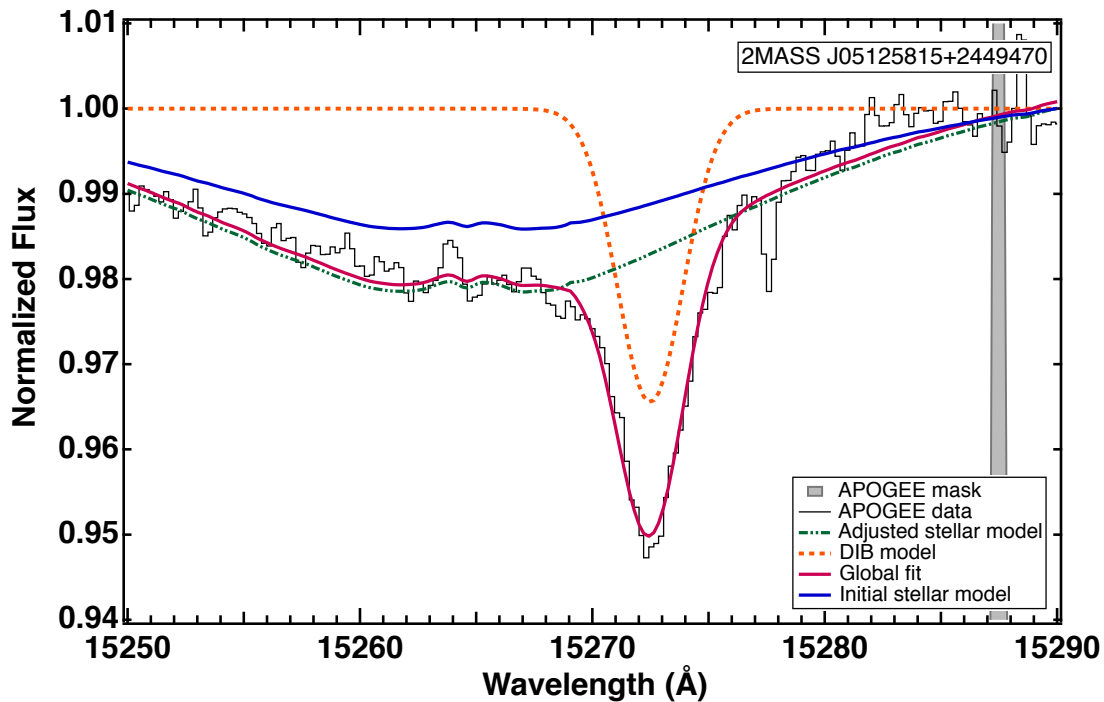


Fig. 1.— Example illustrating our fitting method. Data as provided by the APOGEE survey are shown in black while the final stellar+DIB modeled spectrum appears in magenta. The initial stellar model provided by APOGEE and the model obtained after application of the scaling factor α are shown in solid blue and dash-dot green lines respectively. The DIB absorption alone is represented with a dashed orange line. A grey band in the red part of the spectrum shows an example of masked region.

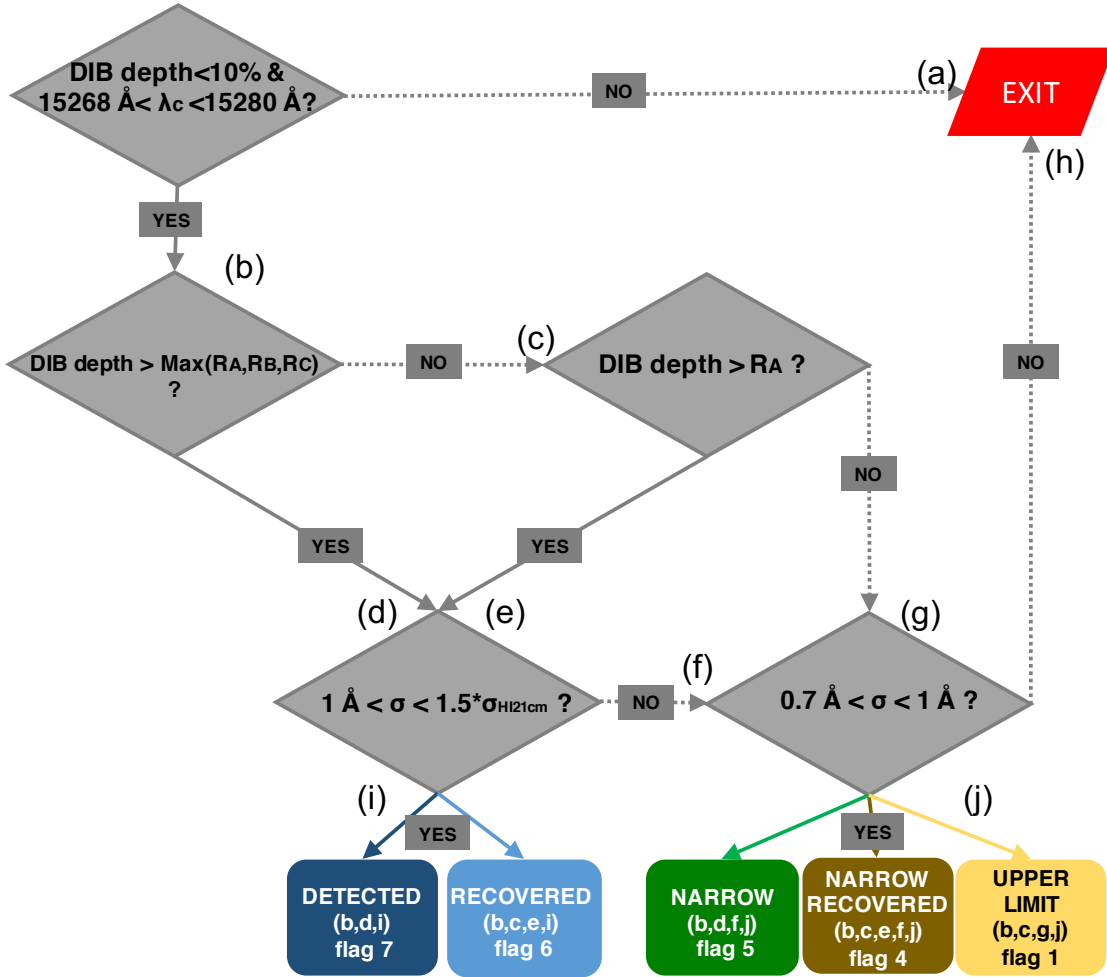


Fig. 2.— Flowchart compiling our decision criteria to create our catalog. Any spectrum able to reach the bottom part of the flow has a positive DIB detection. The path followed by a given spectrum to be classified has been indicated in the corresponding box with small letters. Flags numbers in each box at bottom are detailed in section 5 and included in the catalog.

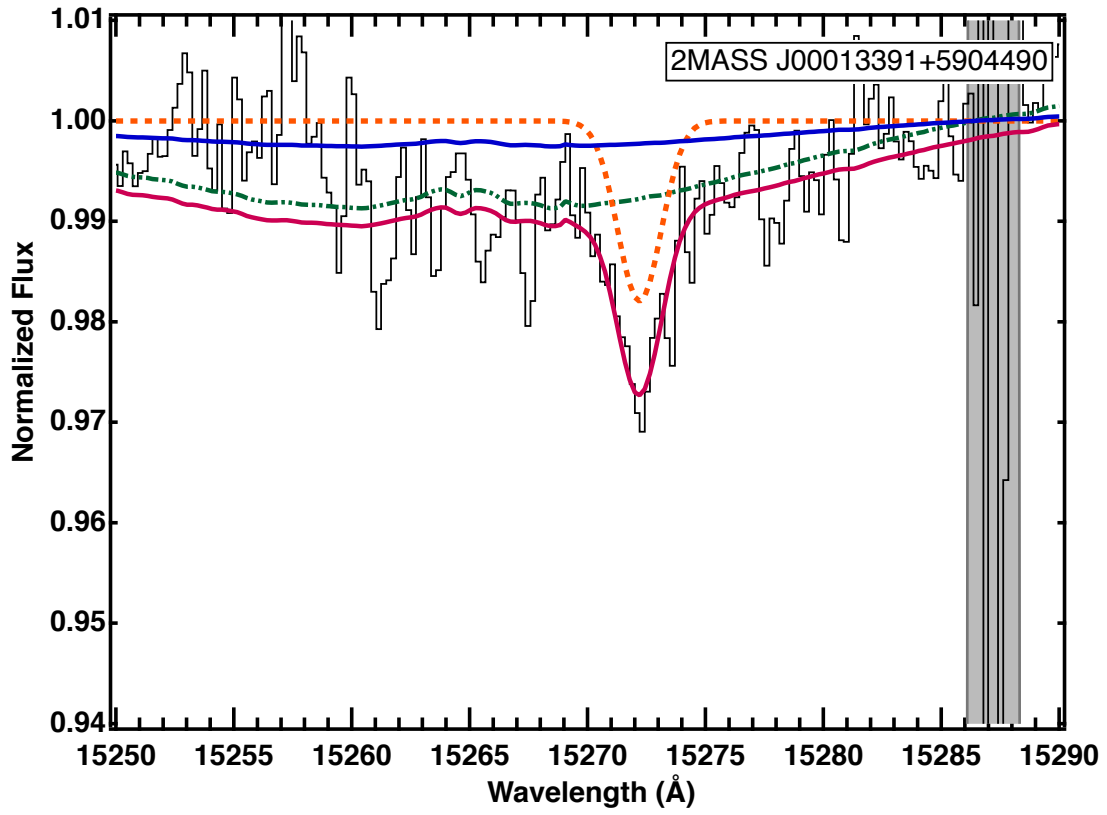


Fig. 3.— Example of detection of narrow DIB ($0.7 \text{ \AA} < \sigma < 1 \text{ \AA}$): 2MASS J00013391+5904490 with $\sigma = 0.9 \pm 0.1 \text{ \AA}$, $\lambda_c = 15272.2 \pm 0.1 \text{ \AA}$ and $EW = 0.041 \pm 0.021 \text{ \AA}$. Color and symbol code is as in Figure 1.

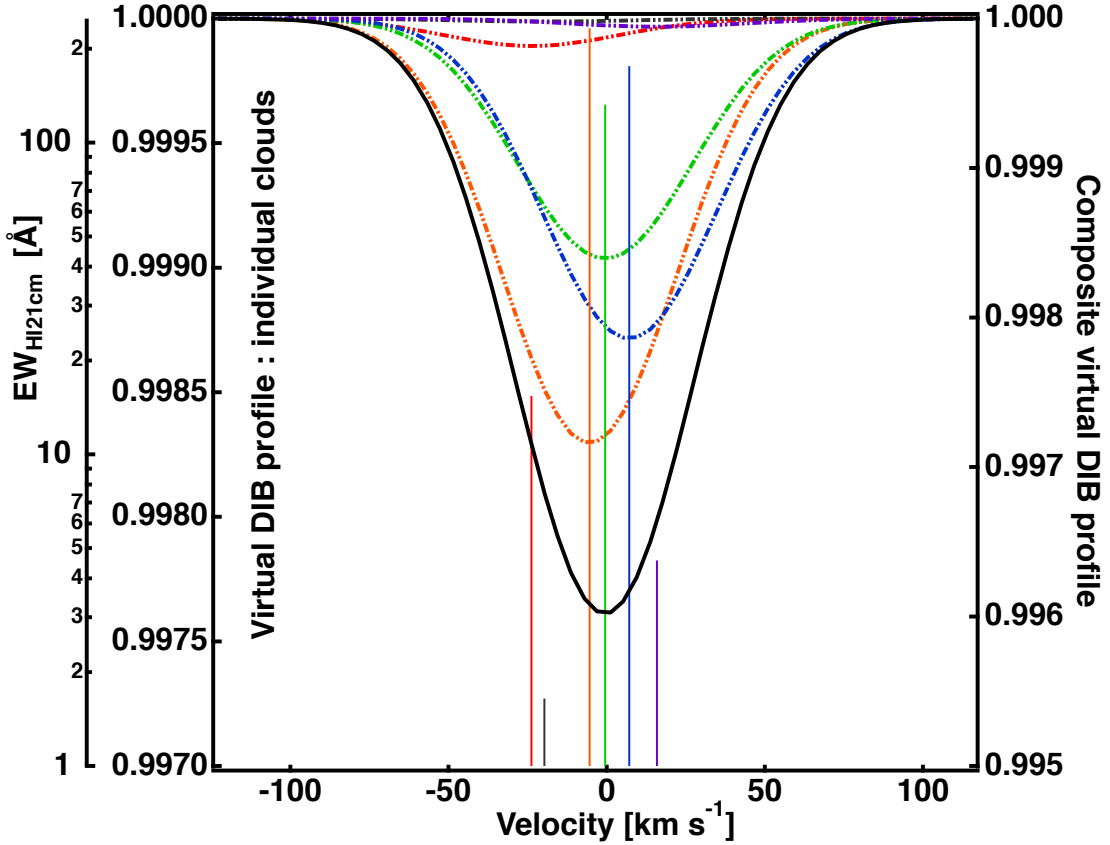


Fig. 4.— Example illustrating our construction of a *virtual* DIB for a typical LOS with 6 HI clouds. Vertical lines in different colors mark the strength and velocity of the 6 individual HI 21cm components. The corresponding individual Gaussians for the synthetic DIBs are shown using the same colors. The function representing the total *virtual* DIB through the HI disk is plotted in black. Note that for a better visualization, the scales for the total DIB and individual components are different.

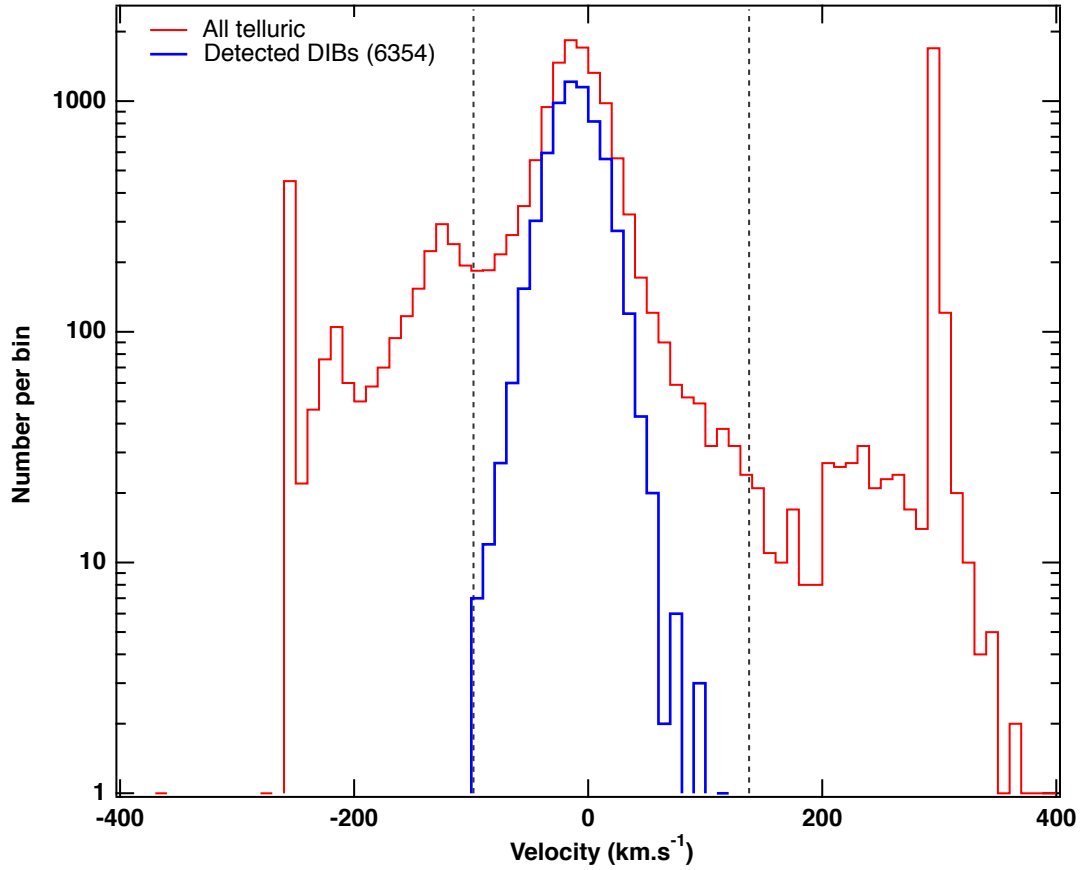


Fig. 5.— Histogram of the Doppler velocities for all fitted lines (red) and for selected DIBs only (blue). The limiting values used in the first selection step are shown as black vertical lines. Note the exclusion of all unrealistic Doppler velocities falling in the first and last bins and the disappearance of the secondary maximum at $\simeq 130 \text{ km s}^{-1}$ that corresponds to false detections produced by a strong stellar line falling at this wavelength.

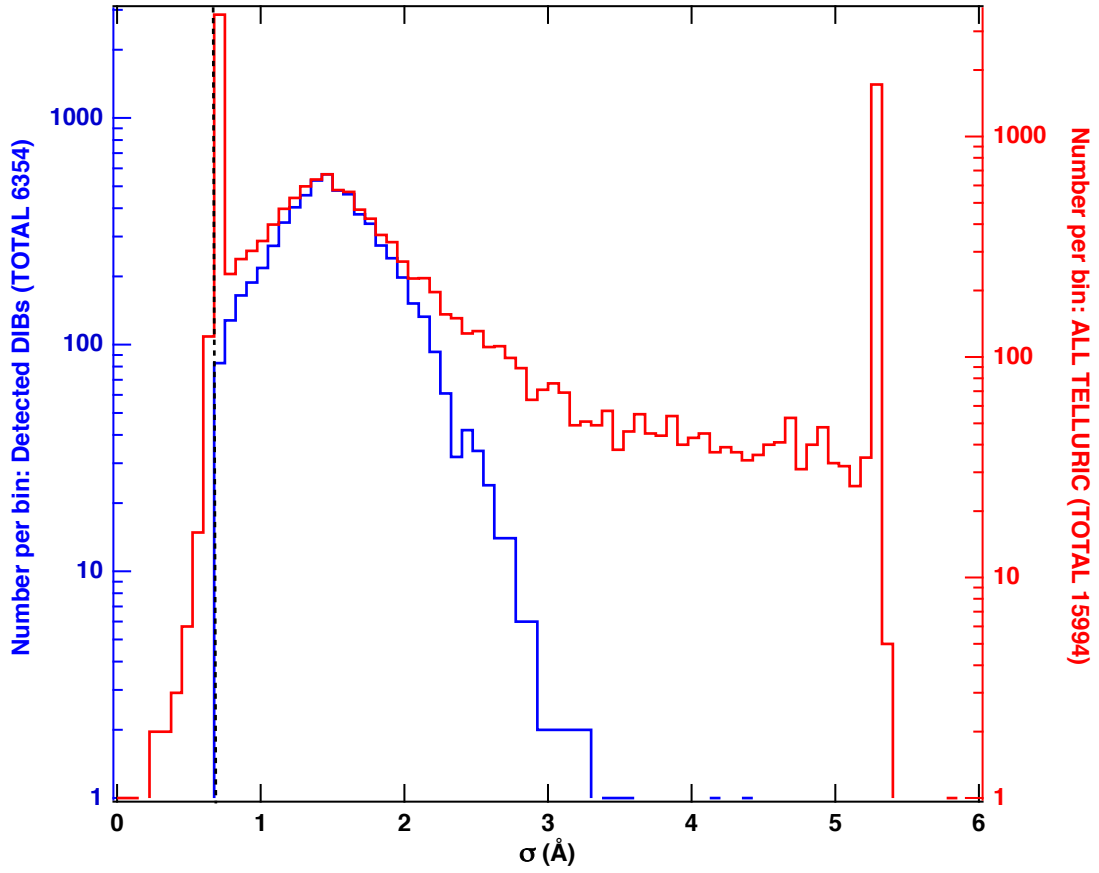


Fig. 6.— Same as Fig 5 for the DIB width σ . The limiting value 0.7\AA used in the selection step is shown as a black vertical line.

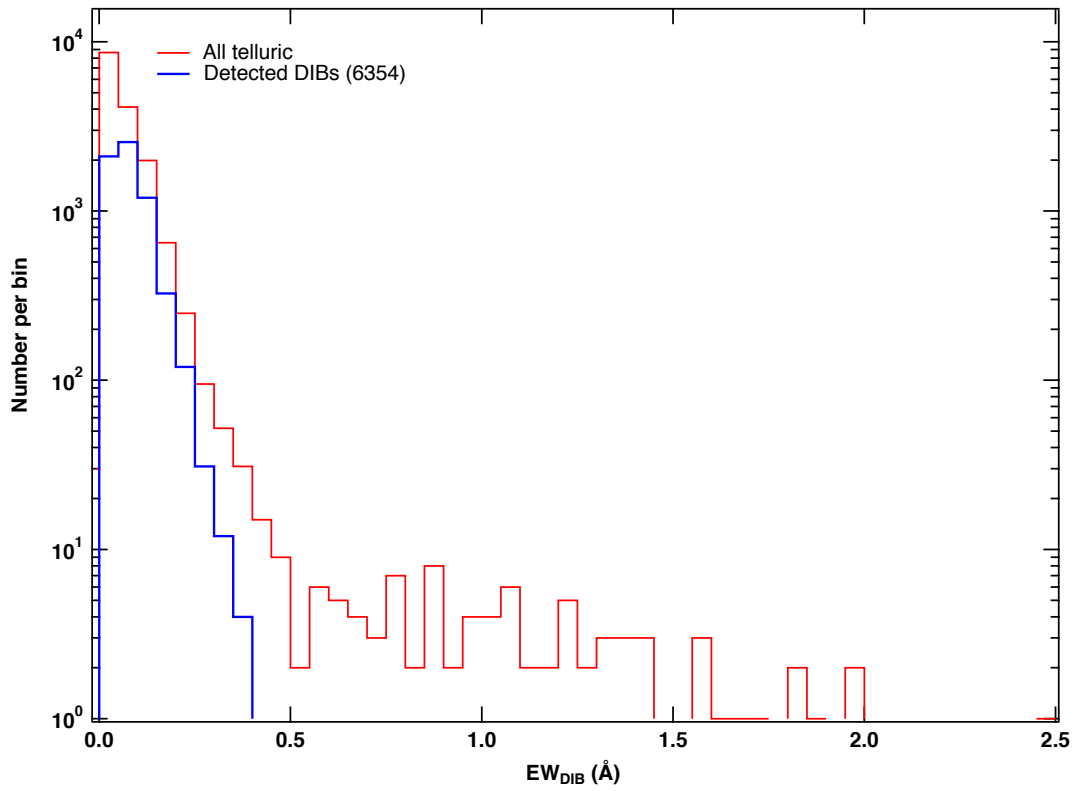


Fig. 7.— Same as Fig 5 for the DIB equivalent width.

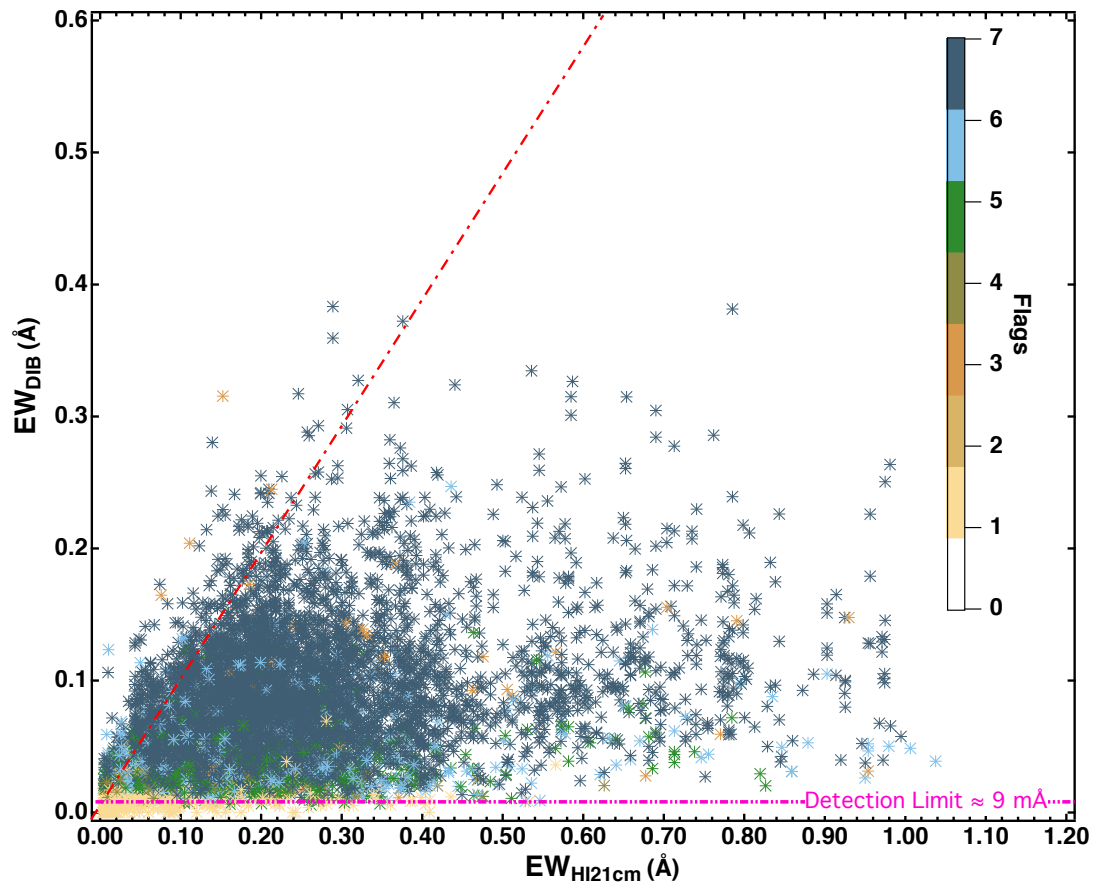


Fig. 8.— DIB equivalent width as a function of the *virtual* DIB equivalent width that is proportional to the total HI column. The dotted red line is the one-to-one relation (see text). The color code is the same as in Fig 2 with 2 additional colors indicating the special cases of Be stars (orange) and stars from field 4529 (camel) from subsection 4.2. A clear detection limit is found at around 9 m\AA indicated by a pink dashed line.

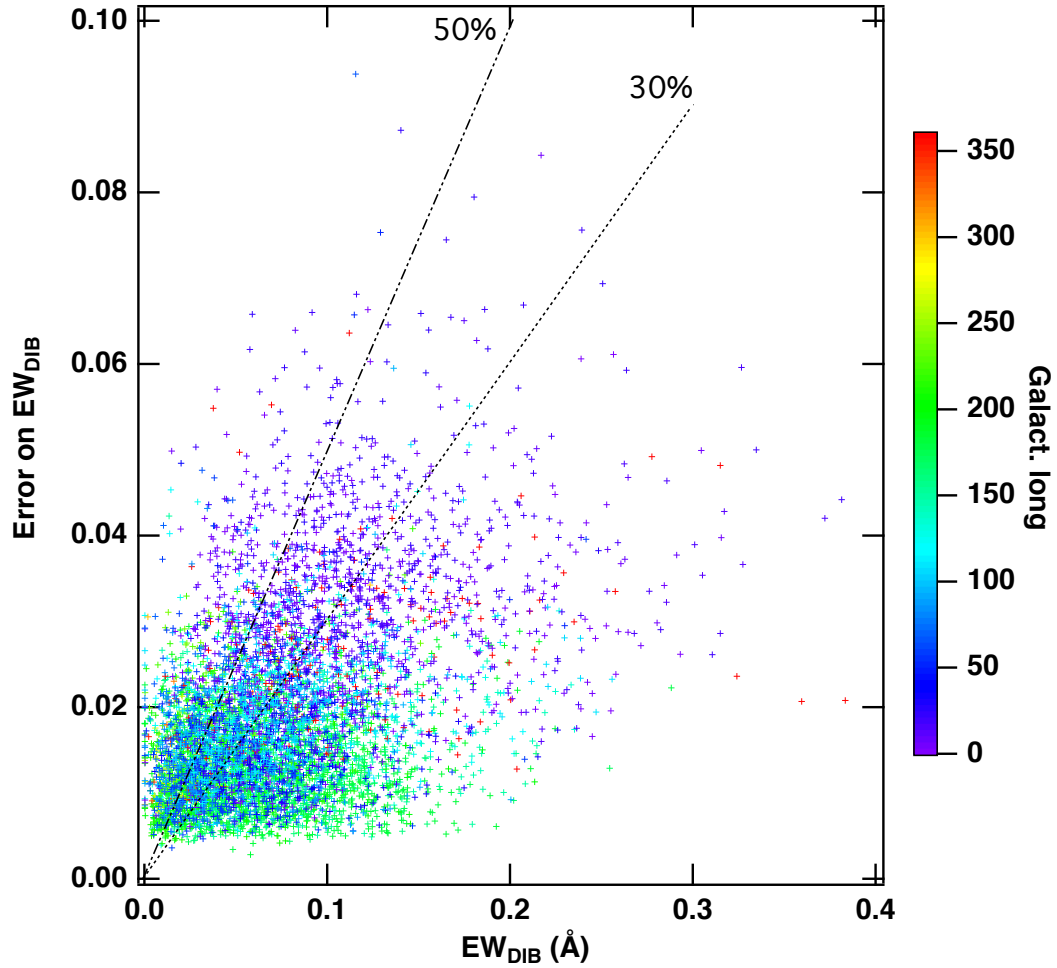


Fig. 9.— Estimated error on the DIB equivalent width EW for all the targets of the catalog. Above (resp. below) dashed lines relative errors are larger (resp. smaller) than 30 and 50 %. The color scale refers to the Galactic longitude of the target star. Due to our method, relative errors are overestimated for targets at lower longitudes (violet, dark blue signs, see text).

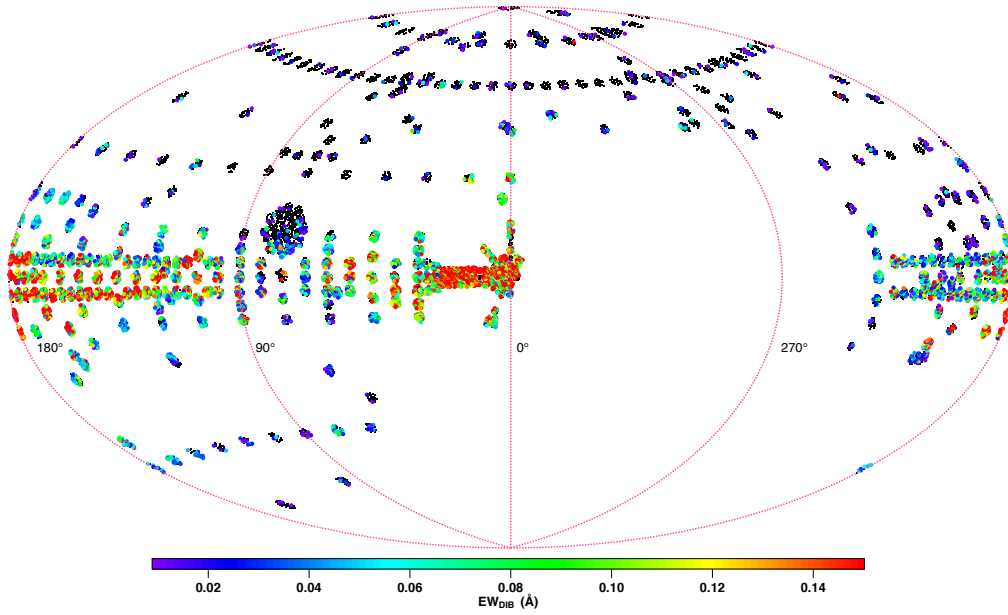


Fig. 10.— Location of all TSS targets on a sky coordinates plot, distinguishing those that are included in the catalog (colored circles, color representative of the EW) from those not included (black circles).

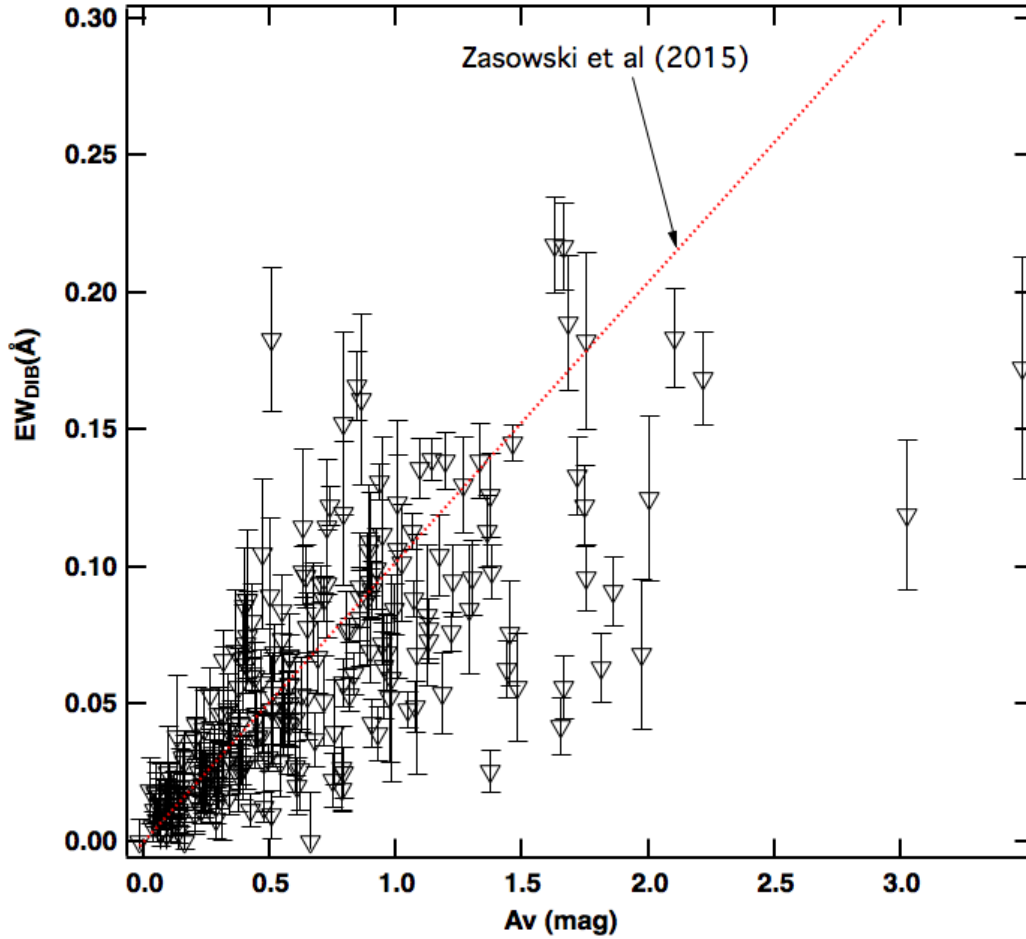


Fig. 11.— DIB equivalent width as a function of the color excess for the subset of 221 targets described in sect. 5. The linear relationship (red curve) is the one fitted to the whole set of APOGEE late-type stars by Zasowski et al. (2015)

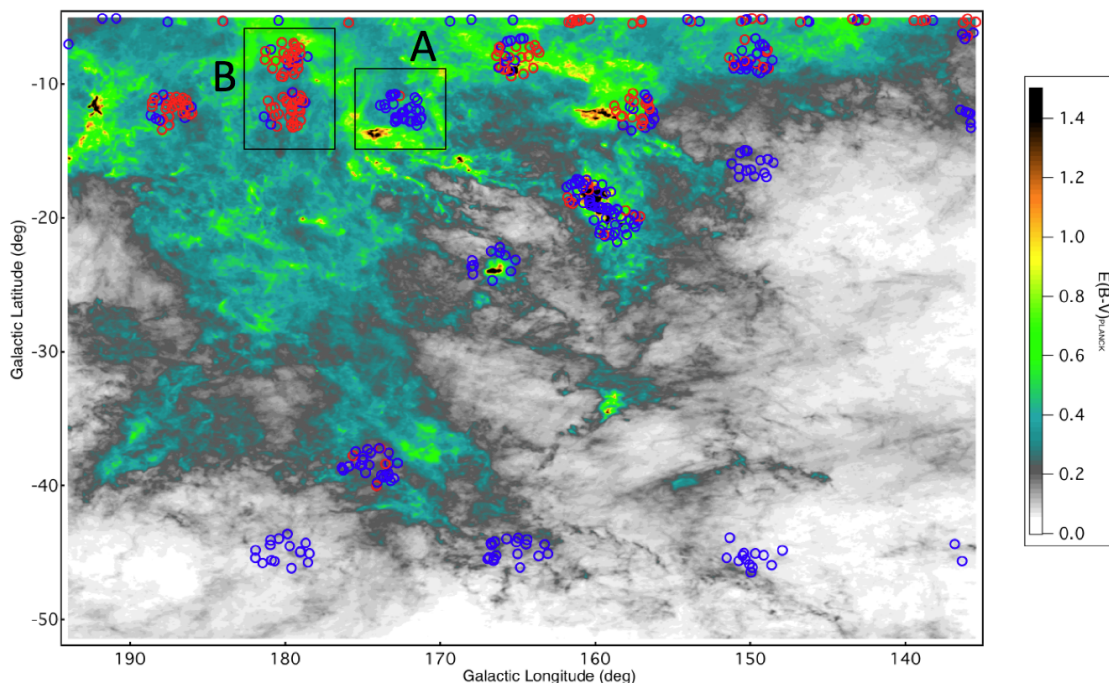


Fig. 12.— Planck dust optical depth in the Taurus-Perseus region with superimposed APOGEE TSS targets selected for the catalog. Blue (resp. red) markers correspond to a DIB equivalent width lower (resp. higher) than a threshold of 50 m\AA . In regions devoid of dust (white or pale grey) DIBs are uniformly below the threshold. Towards dense clouds there is a mixed composition that reflects the location of the target (see Figure 13).

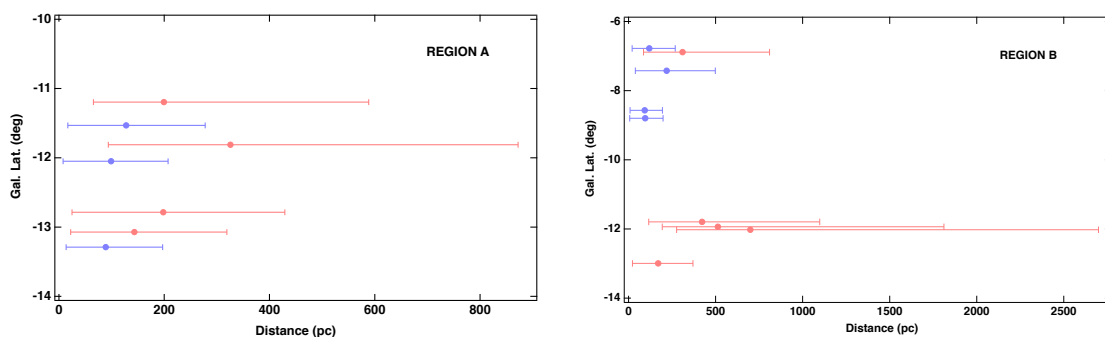


Fig. 13.— Example of future 3D mapping based on DIBs: DIB strengths and target Hipparcos distances for the two regions A and B from Figure 12. Blue (resp. red) markers correspond to a DIB equivalent width lower (resp. higher) than a threshold of 50 m\AA . The closest (resp. most distant) targets show consistently negligible (resp. strong) absorption. Accurate and more numerous parallaxes should allow to bracket the distance to the clouds.

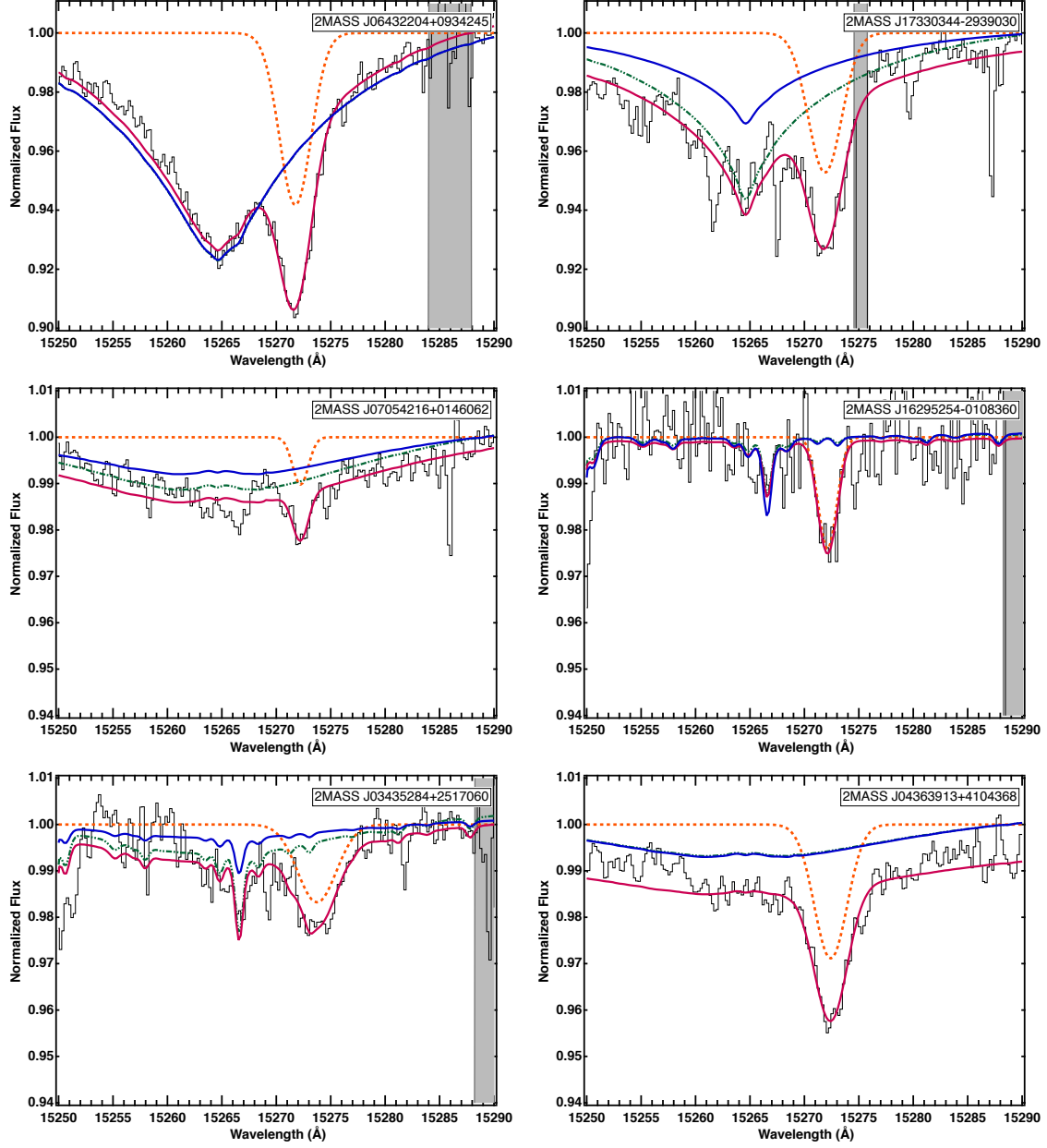


Fig. 14.— Illustration of the various categories of selected absorptions: (Top left) Detected-flag7; (Top right) Recovered-flag6; (Center left) Narrow-flag5; (Center right) Recovered Narrow DIBs -flag4; (Bottom left) Stars from plate 4529 -flag3; (Bottom right) Be Stars -flag2. Color and symbol code is as in Figure 1.